

BAYESIAN ANALYSIS OF HOT JUPITER RADIUS ANOMALIES: EVIDENCE FOR OHMIC DISSIPATION?

DANIEL P. THORNGREN¹ AND JONATHAN J. FORTNEY²

¹*Department of Physics, University of California, Santa Cruz*

²*Department of Astronomy and Astrophysics, University of California, Santa Cruz*

ABSTRACT

The cause of hot Jupiter radius inflation, where giant planets with $T_{\text{eq}} > 1000$ K are significantly larger than expected, is an open question and the subject of many proposed explanations. Rather than examine these models individually, this work seeks to characterize the anomalous heating as a function of incident flux, $\epsilon(F)$, needed to inflate the population of planets to their observed sizes. We then compare that result to theoretical predictions for various models. We examine the population of about 300 giant planets with well-determined masses and radii and apply thermal evolution and Bayesian statistical models to infer the anomalous power as a function of incident flux that best reproduces the observed radii. First, we observe that the inflation of planets below about $M = 0.5 M_{\text{J}}$ appears very different than their higher mass counterparts, perhaps as the result of mass loss or an inefficient heating mechanism. As such, we exclude planets below this threshold. Next, we show with strong significance that $\epsilon(F)$ increases with T_{eq} towards a maximum of $\sim 2.5\%$ at $T_{\text{eq}} \approx 1500$ K, and then decreases as temperatures increase further, falling to $\sim 0.2\%$ at $T_{\text{eff}} = 2500$ K. This high-flux decrease in inflation efficiency was predicted by the Ohmic dissipation model of giant planet inflation but not other models. We also explicitly check the thermal tides model and find that it predicts far more variance in radii than is observed. Thus, our results provide evidence for the Ohmic dissipation model and a functional form for $\epsilon(F)$ that any future theories of hot Jupiter radii can be tested against.

1. INTRODUCTION

The longest standing open question in exoplanetary physics is what causes the inflated radii of “hot Jupiters”, gas giant planets on short period orbits heated to equilibrium temperatures $T_{\text{eq}} > 1000$ K (Miller & Fortney 2011). Since the first detection of planet HD 209458b (Charbonneau et al. 2000; Henry et al. 2000), the radii of the vast majority of these transiting gas giants have exceeded the expected radius of ~ 1.1 times that of Jupiter, sometimes approaching 2 Jupiter radii. This excess radius appears to correlate with the level of incident stellar irradiation (Guillot & Showman 2002; Laughlin et al. 2011), rather than e.g. semi-major axis (Weiss et al. 2013). A wide range of theories have been proposed to explain this, most of which postulate an additional “anomalous” power which heats the convective interior of the planet, leading to larger radii. Typically, these theories are tested by directly modeling the physics to determine if they can produce large enough radii to explain the observations (e.g. Tremblin et al. (2017); Ginzburg & Sari (2016)). We shall take the a more complete approach by determining what anomalous powers are needed to explain the radii of the whole observed population, and then considering what models are most consistent with this.

This approach is feasible thanks to the work of surveys such as WASP, HAT, and Kepler, which have identified a large number of transiting giant planets. Follow-up radial-velocity measurements have yielded mass measurements for many of these. Merging data from the NASA Exoplanet Archive (Akeson et al. 2013) and exoplanet.eu (Schneider et al. 2011), we examine the set of transiting planets with measured masses and radii with relative uncertainties of less than 50%, in the mass range $20 M_{\oplus} < M < 13 M_{\text{J}}$. The resulting flux-radius-mass data is shown in Figure 1. Several patterns are apparent. First, many planets with high incident flux are anomalously large – these are the hot Jupiters. The flux at which this the excess radii become apparent has been estimated to occur at $0.2 \text{ Gerg s}^{-1} \text{ cm}^{-2}$ (Miller & Fortney 2011), equivalent to an equilibrium temperature $T_{\text{eq}} \approx 1000$ K. Second, the degree of radius inflation increases steadily with flux. Finally, the degree of radius inflation is greater at lower masses. This is more visible in Figure 2, which plots radius against planetary mass.

In modeling the interior structure of a transiting giant planet with a measured mass, there are two key variables which are not directly observable: the bulk heavy-element abundance and the anomalous power. Planets at fluxes below the inflation threshold, including Jupiter and Saturn, are well described by evolution models with

zero anomalous power. In this cool giant regime, we can directly infer the heavy-element mass from the observables. Our previous work, Thorngren et al. (2016), did this for the ~ 50 known cool transiting giant planets (those with $T_{\text{eq}} < 1000$ K), and observed a correlation between the planetary heavy-element mass and the total planet mass of $(M_{\text{z}}/M_{\oplus}) \approx 58(M/M_{\text{J}})^{.61}$. That cool giant sample and this hot giant sample do not differ much in semi-major axis (typically $\sim .1$ vs. $\sim .03$ AU), so we do not expect that their formation mechanisms or composition trends to differ. Thus for this work, we apply this relation with its predictive uncertainty as a population-level prior on the heavy-element masses of the hot Jupiters. By doing this, we constrain one of the two unobserved variables, allowing us to infer planetary anomalous power. Individually, planets may vary in composition so by themselves our predictions are not particularly precise. However, since planets as a population will follow the trend line, a hierarchical Bayesian model based on this prior allows us to combine information from our whole sample to infer the shape of the anomalous power as a function of the flux $\epsilon(F)$. The use of the flux as a predictor was suggested by Guillot & Showman (2002) and Weiss et al. (2013), among others.

A key advantage of this approach is that it is robust against certain sources of modeling error. In Thorngren et al. (2016), we discussed the modest systematic uncertainties inherited from the equations of state and the

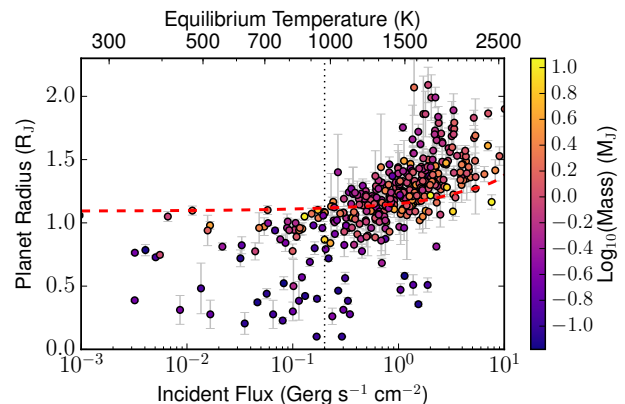


Figure 1. The radii of transiting giant exoplanets plotted against their incident flux (or equilibrium temperature) and colored by mass on the log scale. The dotted red line is the radius of a Jupiter-mass pure H/He model with no inflation effect, an approximate upper limit on the non-inflated case. The dotted vertical line is the empirical flux cutoff for inflation (Miller & Fortney 2011; Demory & Seager 2011). Beyond this level planets are anomalously large, with the excess radius correlated with flux. Less massive planets exhibit the strongest effect.

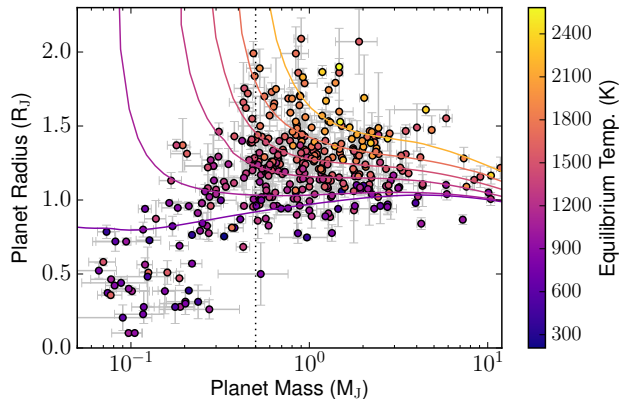


Figure 2. The radii of transiting giant exoplanets plotted against their masses, colored by equilibrium temperature. The solid lines are the radii of model planets of typical composition and inflation power (using our Gaussian Process results described below) for various equilibrium temperatures (815, 1072, 1275, 1449, 1723, and 2166 K) on the same color scale. For each given T_{eq} , models show the radii increasing dramatically at lower masses, coinciding with the absence of planets in that region. This upturn is a feature of any plausible model of anomalous power. Since it seems plausible that a mass-loss process affects this low-mass population, we restrict our study to planets with $M > 0.5M_J$

distribution of metals within the planet (e.g. core vs mixed into the envelope). These issues, as well as statistical uncertainty regarding the mass-metallicity trend and our use of fixed-metallicity atmospheres, could lead to an error in the radius of the model planets. Two factors would act to ameliorate these effects. First, the effects of radius suppression from metallicity would act on planets regardless of temperature, and so the first order errors in deriving the mass-metallicity trend and the impact of metals on hot giant radii would cancel out. Second, because our sample contains a broad cross-section of different masses and fluxes for $M > 0.5M_J$, biases which relate to the planet mass such as atmospheric metallicity are evenly applied to all flux levels. Thus, this type of error may impact the overall magnitude of $\epsilon(F)$, but will have much less effect on the shape of the function. These features do not eliminate systematic error, but they do allow for more confidence in our results.

2. LACK OF INFLATED SUB-SATURNS

An interesting feature is apparent in the mass radius relationship. Figure 2 shows the masses and radii of our sample of planets, along with prediction lines of constant temperature and inflation power. The relationship between the temperature (color) and inflation power is posterior to our model (discussed later), but the general

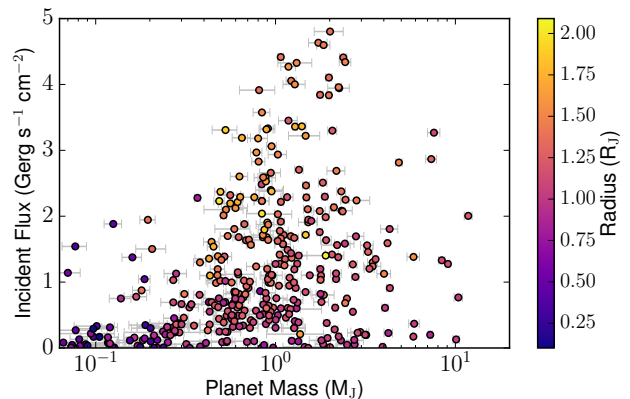


Figure 3. The mass vs. flux of observed transiting giant planets, colored by radius. Below about $0.4 M_J$, considerably fewer high-flux planets are detected, an effect not seen in low-flux planets. Transit observational biases do not explain this. Runaway mass loss could explain both this and the lack of low-mass highly-inflated planets, though biases from formation and migration models might also exist.

shape of the lines themselves is generic, and appears for any mass-independent model of inflation power. It is apparent that with decreasing mass and constant inflation power, the radius anomaly becomes larger exponentially. This is not seen in the observed planet radii. In fact, giant planets are not observed with surface gravity less than about 3 m/s^2 , even though our models allow it and the transits of such large planets would be readily detectable. This might be the result of an inflation mechanism which is inefficient at low masses, but this possibility is weakened by examining the frequency of planets in mass-flux space (see Fig. 3).

Consider the population of high-mass Jupiters compared to lower-mass Saturns, separating the groups at $0.5M_J$. Among Jupiters, many high-flux planets are observed: 58% (164/283) have more than $1 \text{ Gerg s}^{-1} \text{ cm}^{-2}$. Among Saturns, we find only 22% (21/97) which experience this level of insolation. This discrepancy does not appear to result from any observational biases. It is possible that significant mass loss could occur if planets inflate too much. Because radii increase with decreasing mass, any mass loss that occurs might experience positive feedback. This is similar to what was seen in Baraffe et al. (2004), though their mass loss rate appears to have been too high (Hubbard et al. 2007). The best alternative hypothesis appears to be that Saturns preferentially stop migration further from the parent star and that planets at these masses also experience a significantly less efficient inflation effect. Further study will require more advanced models, which we leave to future

work. To avoid this issue, we restrict our attention to planets with $M > 0.5M_J$.

3. PLANET MODELS

Our interior structure models are broadly the same as those in [Thorngren et al. \(2016\)](#), with only two changes for this work on inflated giant planets. We solve the equations of hydrostatic equilibrium, conservation of mass, and an equation of state (EOS) based on the SCvH ([Saumon et al. \(1995\)](#)) solar H/He EOS and the EOS of a 50/50 ice/rock mixture ([Thompson 1990](#)).

$$\frac{\partial P}{\partial m} = -\frac{Gm}{4\pi r^4} \quad (1)$$

$$\frac{\partial r}{\partial m} = \frac{1}{4\pi r^2 \rho} \quad (2)$$

$$\rho = \rho(P, T) \quad (3)$$

Metals were fully mixed into the convective envelope using the additive volumes approximation. No core was included because for planets of this mass the radius difference would be minor (see [Thorngren et al. \(2016\)](#)). Heat flow out of the planet (and therefore thermal and structural evolution) was regulated using the atmospheric models of [Fortney et al. \(2007\)](#). Additional details and analysis of the effect of our modeling choices can be found in [Thorngren et al. \(2016\)](#). Sample evolution calculations are shown in [Figure 4](#).

The most important modeling addition is the inclusion of an additional heating power $\epsilon F \pi R^2$. The resulting power balance of the interior of the planet is

$$\frac{\partial E}{\partial t} = \pi R^2 (\epsilon F - 4L_{int}) \quad (4)$$

Here L_{int} is the intrinsic luminosity of the planet as computed by the atmosphere model. Note that our definition of ϵ differs slightly from other authors, such as [Komacek & Youdin \(2017\)](#), who deposit the energy at a particular depth within the planet. Using their results, our definitions agree for their models where the power is deposited at the radiative-convective boundary or deeper. Otherwise, our ϵ is smaller than theirs by a factor < 1 depending on depth and stage of evolution.

The other change was an improvement to the thermal evolution integration system. The new system uses the SciPy ([Van Der Walt et al. 2011](#)) function Odeint to adaptively integrate the changes in planet internal entropy. We have also added a system to detect when the planet is near thermal equilibrium (when $\epsilon F \pi R^2 \approx L_{int}$), and quickly completes the evolution accordingly. This serves to handle the stiffness of the ODE near an equilibrium of high specific entropy.

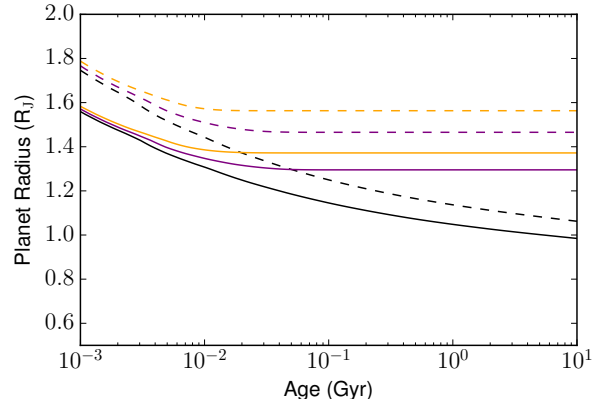


Figure 4. Example outputs of our evolution models for a $1 M_J$ planet at $2 \text{ Gerg s}^{-1} \text{ cm}^{-2}$ for different heavy-element masses and values of heating efficiency. Solid and dashed lines have 60 and 30 M_{\oplus} of heavy elements respectively, and black, purple, and orange lines have 0, 1, and 2% heating efficiencies respectively. The plot extends to extremely young ages to illustrate the transition from rapidly cooling young planets to the nearly static older planets. Planets in our sample are generally older than a gigayear, so the effects of the heavy-element abundance and heating efficiency are not easily disentangled.

4. BAYESIAN STATISTICAL ANALYSIS

Our statistical analysis is based on a hierarchical Bayesian approach, with two levels in the hierarchy. The lower level consists of our beliefs about the properties of individual planets given the observations and our planetary mass-metallicity relation from [Thorngren et al. \(2016\)](#) as a prior on bulk metallicity. The upper level combines information about the individual planets to infer population level patterns in anomalous power.

4.1. Planetary Statistical Models

For each planet in our sample, there is a set of observations which define our knowledge of the planet's properties. These are the observed mass, radius, age, and average incident flux, as well as the associated uncertainties. For convenience of notation, we group all this known information together as the variable \vec{y}_i .

$$\vec{y}_i = [M_{\text{obs},i}, \sigma_{M,i}, R_{\text{obs},i}, \sigma_{R,i}, t_{\text{min},i}, t_{\text{max},i}, F_i] \quad (5)$$

Our structural evolution models give us radii as a function of the planet mass, metal mass, flux, anomalous power, and age. This model relates not to the observed planet properties, but the true (and unknown) values of these properties. We will denote these variables collectively as $\vec{\theta}_i$, which includes some values for which we have no direct information ($M_{z,i}$ and ϵ_i). The true radius R_i , is not a parameter, but rather a deterministic

function of the others (computed from our physical models).

$$\vec{\theta}_i = [M_i, M_{z,i}, \epsilon_i, t_i] \quad (6)$$

$$R_i = R(M_i, M_{z,i}, F_i, \epsilon_i, t_i) \quad (7)$$

Our observations are derived from these true properties, and the uncertainties thereof are a product of the observational process.

$$M_{\text{obs},i} \sim \mathcal{N}(M_i, \sigma_{M,i}^2) \quad (8)$$

$$R_{\text{obs},i} \sim \mathcal{N}(R_i, \sigma_{R,i}^2) \quad (9)$$

$$t_i \sim \mathcal{U}(t_{\text{min},i}, t_{\text{max},i}) \quad (10)$$

Here $\mathcal{N}(\mu, \sigma^2)$ is the normal distribution with mean μ and variance σ^2 , and $\mathcal{U}(a, b)$ is the uniform distribution between a and b . This separation of the observation (a constant) from the true value (a variable) is done to allow a proper accounting of their uncertainties in the model. In this sense, M_i , and t_i are nuisance parameters, and we are only interested in their effect on the unobserved ϵ_i . We do not expect to learn more about the planet mass from this model, and indeed we see that in general the marginal posterior of $M_i \approx \mathcal{N}(M_{\text{obs},i}, \sigma_{M,i}^2)$.

In addition, we have a motivated prior belief as to the planet's metal content from [Thorngren et al. \(2016\)](#).

$$p(M_{z,i}|M_i) = \mathcal{LN}(\alpha + \beta \log_{10}(M_i), \sigma_z^2) \quad (11)$$

Here $\mathcal{LN}(\mu, \sigma^2)$ is the base-10 log-normal distribution with location μ and scale σ^2 (i.e. the \log_{10} of the variable is distributed as $\mathcal{N}(\mu, \sigma^2)$). We use the median values from [Thorngren et al. \(2016\)](#) for α , β , and σ_z^2 . Setting the remaining priors $\propto 1$, we can apply Bayes' rule to write down the posterior up to a proportionality constant. This gives us our belief about the planet's parameters $\vec{\theta}_i$ given the observations.

$$p(\vec{\theta}_i|\vec{y}_i) = p(\vec{y}_i|\vec{\theta}_i)p(\vec{\theta}_i)/p(\vec{y}_i) \quad (12)$$

$$p(\vec{\theta}_i|\vec{y}_i) \propto \mathcal{N}(M_{\text{obs},i}|M_i, \sigma_{M,i}^2) \times \quad (13)$$

$$\mathcal{N}(R_{\text{obs},i}|(R(M_i, M_{z,i}, F_i, \epsilon_i, t_i), \sigma_{R,i}^2) \times$$

$$\mathcal{U}(t_i|t_{\text{min},i}, t_{\text{max},i}) \times$$

$$\mathcal{LN}(M_{z,i}|\alpha + \beta \log_{10}(M_i), \sigma_z^2)$$

Consistent with the usual Bayesian statistical notation, $\mathcal{N}(x|\mu, \sigma^2)$ is the PDF of $\mathcal{N}(\mu, \sigma^2)$ evaluated at x (similarly for \mathcal{U} and \mathcal{LN}). This completes the lower level of the model. An example posterior for HD 209458 b is shown in figure 5.

4.2. Models of Anomalous Power

In the previous section, we have described a model of planets which are independent of one another. Here, in the upper level of the hierarchical model, we will unify this information to learn about the function $\epsilon(F)$. We can do this within a Bayesian context by considering a prior on $\vec{\theta}$ which is the product of two independent terms: the mass-metallicity relation given earlier, and a function for ϵ from the known value of F and some new hyperparameters. For convenience, we will continue to use the notation $p(\vec{\theta}_i|\vec{y}_i)$ to refer to the terms defined in equation 13, even though it is not strictly speaking a posterior anymore, as there is an additional portion of the prior which is not included.

We will consider several forms of the function $\epsilon(F)$: a Gaussian process (GP) in $\log_{10}(\epsilon)$ for a general shape (ϵ_{GP}), a step-function shape (ϵ_s), a power-law shape (ϵ_p) a logistic shape (ϵ_l), and a Gaussian shape (ϵ_g).

$$\log_{10}(\epsilon_{GP}(\vec{F})) \sim GP(0, \mathbf{K}(\vec{F})) \quad (14)$$

$$\epsilon_s(F) = \begin{cases} 0 & \text{for } F < F_0 \\ \epsilon_{\text{max}} & \text{for } F \geq F_0 \end{cases} \quad (15)$$

$$\epsilon_p(F) = F_0 F^k \quad (16)$$

$$\epsilon_l(F) = \frac{\epsilon_{\text{max}}}{1 + (F/F_0)^{-k}} \quad (17)$$

$$\epsilon_g(F) = \epsilon_{\text{max}} \exp\left(-\frac{\log_{10}(F/F_0)^2}{2s^2}\right) \quad (18)$$

For the parametric models, $\epsilon(F)$ is a deterministic function of flux. Let the fit parameters for these models be $\vec{\phi}$, for which each model will be slightly different.

$$\vec{\phi}_s = [\epsilon_{\text{max}}, \log_{10}(F_0)] \quad (19)$$

$$\vec{\phi}_p = [\epsilon_0, k] \quad (20)$$

$$\vec{\phi}_l = [\epsilon_{\text{max}}, F_0, k] \quad (21)$$

$$\vec{\phi}_g = [\epsilon_{\text{max}}, \log_{10}(F_0), s^2] \quad (22)$$

With this notation, we can write down the likelihood for a given model as the the product of the likelihoods of each individual planet given that $\epsilon_i = \epsilon(F, \vec{\phi})$. In this way, we are simply searching through the space of parameters $\vec{\phi}$ which produce planet models which are most consistent with the observed parameters of the planets in our sample. All of our parameter priors are $p(\vec{\phi}) \propto 1$ except for the logistic model, where $p(\vec{\phi}_l) \propto \mathcal{N}(k|4, 2)$, which was needed to avoid an identifiability issue that occurs when k becomes large. This prior is not very informative - it merely asserts that the scale of the logistic transition should be similar to the scale of the data.

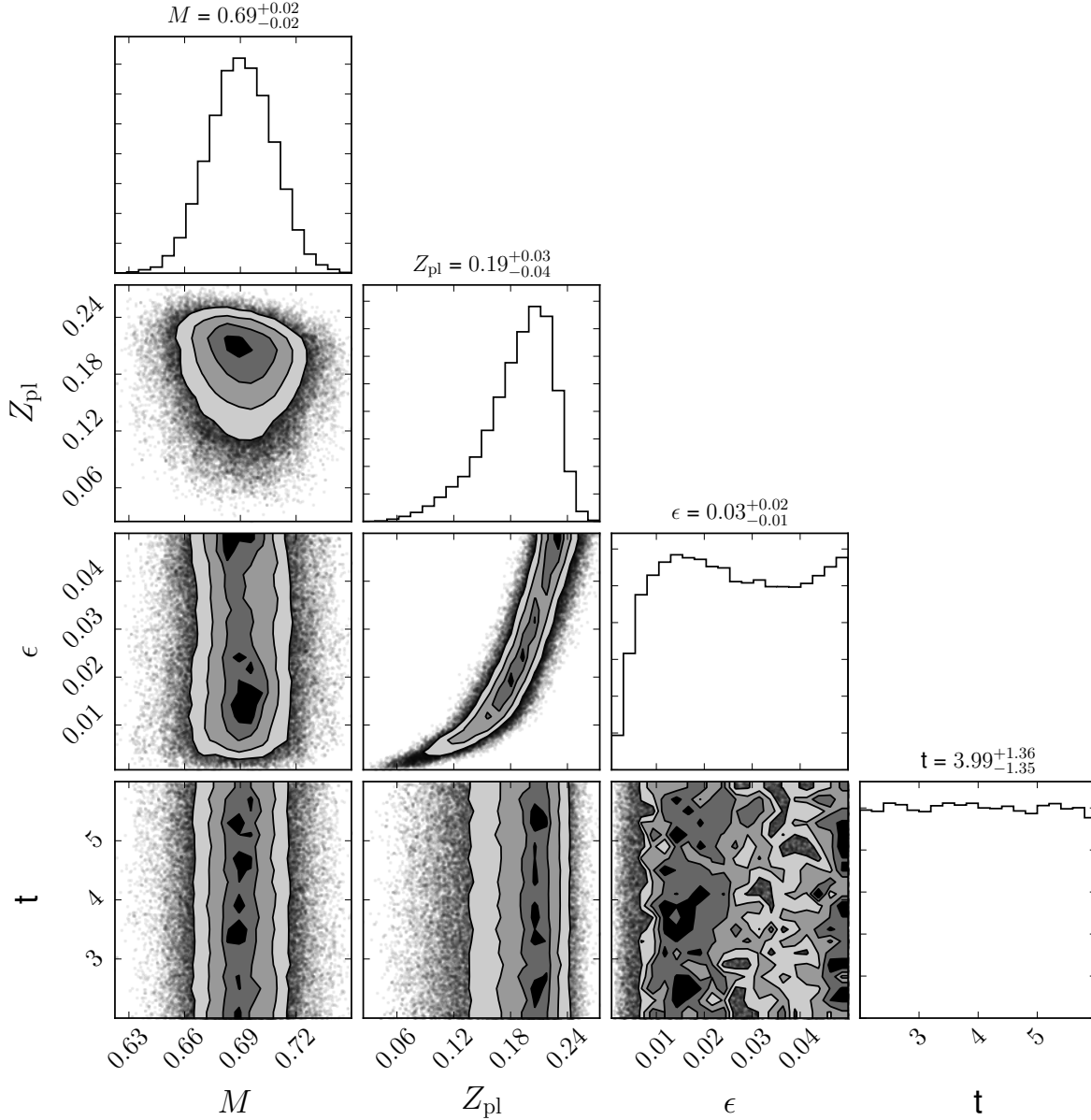


Figure 5. Inferred parameters for HD 209458 b, using equation 13. The parameters are mass in Jupiter masses, planetary metal mass fraction, inflation efficiency, and age in gigayears. The planet is old enough that its age uncertainty has little effect on the other parameters. As expected, the main driver of ϵ uncertainty is Z_{pl} . For this planet, we disfavor an inflation efficiency below $\sim 1\%$. Together with other planets, some of which disfavor high ϵ , this forms the basis for our inference of $\epsilon(F)$.

Thus, our full posterior probabilities for the parametric models are:

$$p(\vec{\phi}|\mathbf{y}) = p(\mathbf{y}|\theta)p(\theta|\vec{\phi})p(\vec{\phi})/p(\mathbf{y}) \quad (23)$$

$$\propto p(\vec{\phi}) \prod_{i=1}^N p(\vec{y}_i|\vec{\theta}_i)p(\vec{\theta}_i)\delta(\epsilon_i - \epsilon(F_i, \vec{\phi})) \quad (24)$$

$$\propto p(\vec{\phi}) \prod_{i=1}^N p(\vec{\theta}_i|\vec{y}_i)\delta(\epsilon_i - \epsilon(F_i, \vec{\phi})) \quad (25)$$

Each of these terms has been defined, and in particular, $p(\vec{\theta}_i|\vec{y}_i)$ is given in Equation 13. Also recall that ϵ_i is the third component of $\vec{\theta}_i$. The delta function $\delta(\epsilon_i - \epsilon(F_i, \vec{\phi}))$ is the $p(\theta|\vec{\phi})$ term, and represents the constraint that each planet's ϵ_i is given deterministically by the function $\epsilon(F, \vec{\phi})$ for a given ϕ . This completes our description of the parametric models.

The GP model differs somewhat from the parametric models in that it includes an intrinsic spread σ_2^2 , such that $\epsilon(F)$ is random, even for fixed F and parameters. This spread is included to make the problem more

computationally tractable, but is fixed at a small value $\sigma_2^2 = .001$, which amounts to a $\sim 7\%$ relative spread in linear space. Nevertheless this produces significant changes to the structure of the parameters and the likelihood. We use a Gaussian covariance function with white noise, so the parameters of the process are the correlated variance and length scale.

$$\mathbf{K}_{i,j}(\vec{\phi}_{GP}) = \sigma_1^2 \exp\left(-\frac{\log_{10}(F_i/F_j)^2}{2l^2}\right) + \sigma_2^2 \delta_{i,j} \quad (26)$$

$$\vec{\phi}_{GP} = [\log_{10}(l), \log_{10}(\sigma_1^2)] \quad (27)$$

Because the values of ϵ_i are not fixed, even given ϕ , it is necessary to explicitly include these as parameters, which we will refer to as $\vec{\epsilon}$ (equivalent to θ). Additionally, the likelihood of the GP is computed as a function of $\vec{\epsilon}$ all at once, rather than simply being a delta function as with the parametric case. We set the prior $p(\vec{\phi}) \propto 1$. The result of all of this is the following posterior probability:

$$p(\vec{\phi}|\mathbf{y}) = p(\mathbf{y}|\theta)p(\theta|\vec{\phi})p(\vec{\phi})/p(\mathbf{y}) \quad (28)$$

$$\propto p(\vec{\theta})p(\vec{\phi})GP(\log_{10}(\vec{\epsilon})|\vec{0}, \mathbf{K}(\phi)) \prod_{i=1}^N p(\vec{y}_i|\vec{\theta}_i)p(\vec{\theta}_i) \quad (29)$$

$$\propto \mathcal{LN}(\vec{\epsilon}|\vec{0}, \mathbf{K}(\phi)) \prod_{i=1}^N p(\vec{\theta}_i|\vec{y}_i)p(\epsilon_i) \quad (30)$$

Note that we have a new prior on $\vec{\epsilon}$; in the parametric case, this was set $\propto 1$. Adding anomalous power at 0.1%, 1%, or 3% below about $F \approx 10^8$ makes little difference to the radius because there is simply not enough power to inflate the planet to a detectable degree. As such, we apply this prior to serve as a soft lower boundary condition based on the belief that the anomalous power is roughly zero for smaller values of stellar insolation.

$$p(\log_{10}(\epsilon_i)) \propto \begin{cases} 1 & \text{for } F_i \geq 10^8 \\ \mathcal{LN}(\epsilon_i | -3, 1) & \text{for } F_i < 10^8 \end{cases} \quad (31)$$

Ultimately, experimentation shows that this prior has little effect on the values or shape of the resulting function for $F > 2 \times 10^8$, from which we draw our science conclusions. We include it merely to best represent our beliefs about the function for the full range of fluxes.

Finally, we constructed a simple model for the thermal tides model of hot Jupiter inflation (Arras & Socrates 2009). We adapt the scaling relations of Socrates (2013), $L \propto T_{eq}^3 R^4 P^{-2}$, where L is the total anomalous power, P is the period, T_{eq} is the equilibrium temperature,

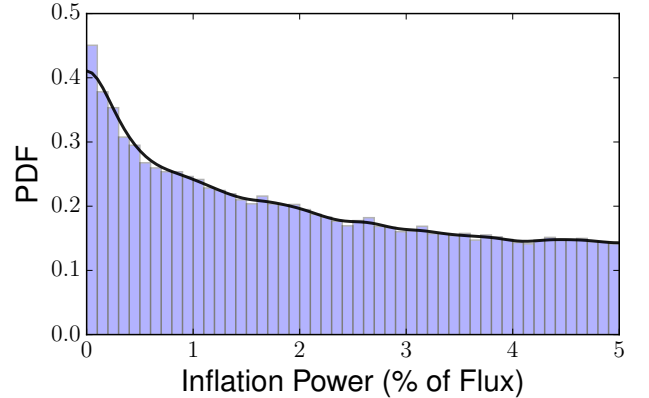


Figure 6. The histogram and kernel density estimate (the black line) of the posterior inflation power ϵ of WASP-43 b. In this case, smaller values of ϵ are more likely, but larger values are not ruled out. Note that the KDE matches the histogram, as is required for us to be able to use it as a likelihood for the upper level of the hierarchical model.

and R is the planet radius. We model this as $\epsilon = \epsilon_0 R^2 P^{-2} F^{-.25}$, where ϵ_0 is a model parameter. We use the present-day radius and flux for simplicity.

4.3. Statistical Computation

To efficiently sample the posteriors described in Section 4.1, we divide the problem into two steps – computing the function $p(\vec{\theta}_i|\vec{\phi})$ for each planet i using equation 13, then agglomerating these data into a posterior in ϕ using equations 25 and 30. In a general hierarchical model this sort of factorization would not be feasible, but our case is amenable to it because the only link between the lower (Eq. 13) and upper (Eq. 25 & 30) parts of the hierarchy is $p(\epsilon_i|\vec{y}_i)$. This is simply $p(\vec{\theta}_i|\vec{y}_i)$ with the other variables M_i , $M_{z,i}$, and t_i marginalized out.

To take advantage of this, we run a Metropolis-Hastings MCMC (Hastings (1970)) on Equation 13 for each planet, recording 100,000 samples of each ϵ_i on $0 < \epsilon_u < 5\%$. This limit at 5% can be interpreted as a prior; we do not expect heating efficiency to rise past this for theoretical reasons and because it is not necessary to explain any observed planet. This has no significant effect on any model, except for the power-law model, which is strongly disfavored anyway. We then apply a Gaussian kernel density estimate (KDE) with reflected boundaries (see Silverman (1986)) to derive easily interpolable functions. It should be noted that while these values can be treated like a posterior from the perspective of the lower level, they are in fact a likelihood from the perspective of inferring $\vec{\phi}$ – this is the nature of a hierarchical Bayesian model. From this point on, we may compute the upper level with a single Metropolis-Hastings run. Whenever we need to compute

$p(\vec{\epsilon}_i|\vec{y}_i)$, we can simply look up the value of the appropriate location in our table of KDE-derived functions. This will return a value which is merely proportional to $p(\vec{\epsilon}_i|\vec{y}_i)$, but the constant of proportionality cancels out in the MCMC calculation. Scatterplot matrices of our upper-level model posteriors are shown in figures 7-10, and the those of the lower level model for HD 209458 b are shown in figure 5. The plots were made using corner.py (Foreman-Mackey (2016)).

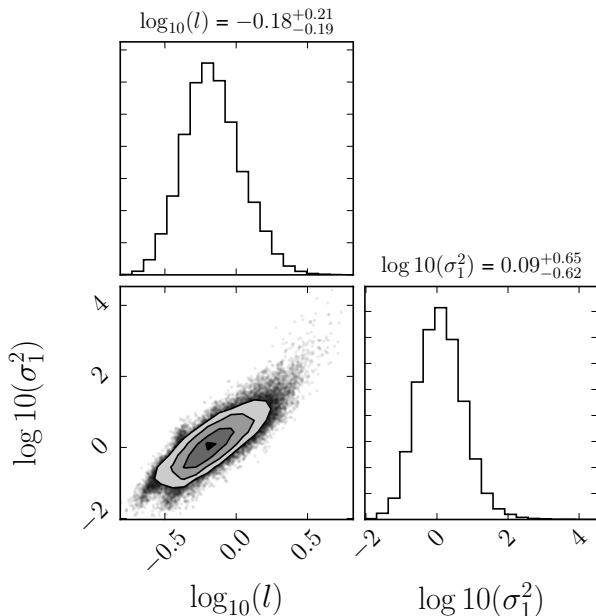


Figure 7. A scatterplot matrix of the GP hyperparameter posterior (see eq. 26). It is fairly well-behaved, but has a long right tail. This is a common feature for Gaussian processes.

To compare different models, we are unable to use the more familiar Bayesian model selection criteria, the BIC/AIC, as these are only defined for non-hierarchical models. This is because in the hierarchical case the number of parameters is not well-defined (Gelman et al. 2014). Instead, we make use of the Deviance Information Criterion (DIC), which is similar to the AIC in interpretation, but which makes use of an estimate of the effective number of parameters (Spiegelhalter et al. 2002), derived from the variance of the log posterior likelihood. The empirical DIC from a set of samples is:

$$\text{DIC} = -2 \log(p(\mathbf{y}|\hat{\epsilon})) + 4 \text{Var}_s [\log(p(\mathbf{y}|\vec{\epsilon}_s))] \quad (32)$$

Here, $\hat{\epsilon}$ is the posterior mean of $\vec{\epsilon}$ and Var_s is the variance of the log likelihood across samples. Note that while the samples in question are taken using the posterior, this computation is done using the likelihood. In

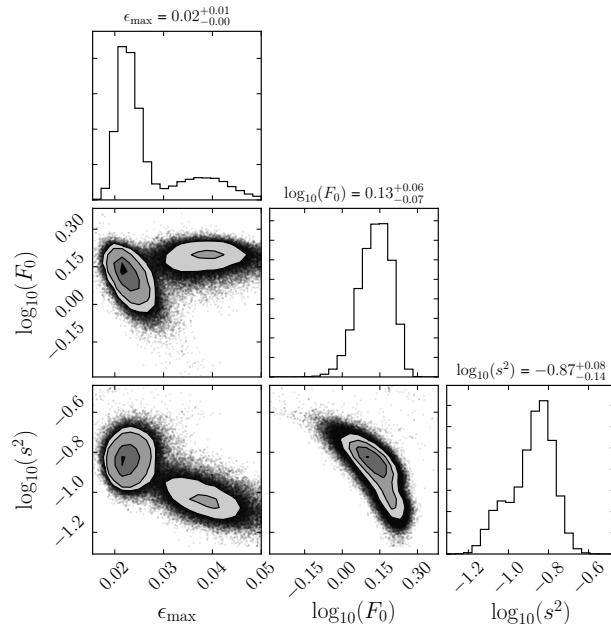


Figure 8. A scatterplot matrix of the Gaussian function hyperparameter posterior (see eq. 18). Two modes were observed, differing primarily in height ϵ_{\max} ; the model with a peak of $\epsilon \approx 2\%$ is favored over the model with peak $\epsilon \approx 3.5\%$ by a probability ratio of about 75% to 25%. The discovery of more giant planets around the ≈ 1500 K peak will help to resolve this further.

the results, the model with the more negative DIC is favored. The interpretation of ΔDIC is similar to that of the AIC and BIC, in which differences of $>\sim 6$ are strong evidence in favor of the model with the lesser DIC (e.g. Kass & Raftery (1995) for BIC).

To make predictions of planet radius, we simply sample from the function $R(M_i, M_{z,i}, F_i, \epsilon_i, t_i)$ given the planet parameters we are interested in. For the case of producing mass-flux-radius relation predictions, M_i , F_i , and t_i are taken as fixed, M_z is drawn from Equation 11. For ϵ_i , we do the usual posterior predictive approach: take draws from $\epsilon(F, \vec{\phi})$ marginalized over the posterior $p(\vec{\phi}, \mathbf{y})$. The result is a probability distribution in R for the given parameters.

5. RESULTS

The results for $\epsilon(F)$ are shown in Figure 11. All functional forms yield similar results below about $0.5 \text{ Gerg s}^{-1} \text{ cm}^{-2}$, but differ significantly above this. The GP model reaches a peak at around 1600 K and decreases towards zero with high statistical confidence, as shown by the uncertainty bounds. At high fluxes, the uncertainty in heating power is roughly constant, and so declines as a fraction of flux. Figure 2 shows the predicted radius for a given mass of 5 Gyr old planets of average com-

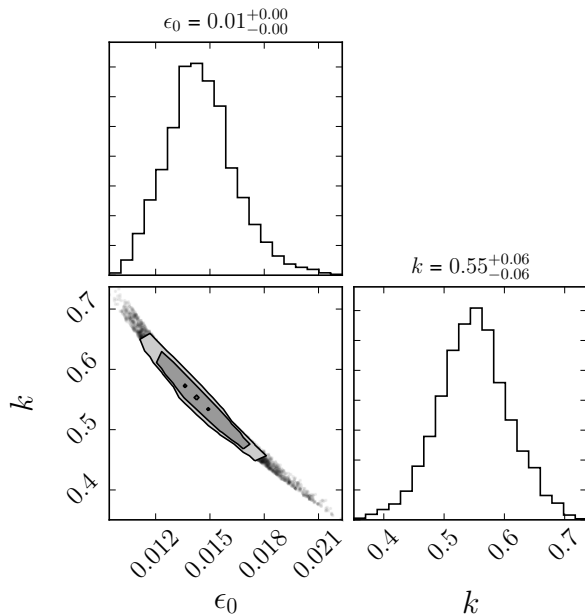


Figure 9. A scatterplot matrix of the power law hyperparameter posterior (see eq. 16). A strong correlation between the coefficient F_0 and the power k is seen. This likely reflects the constraint that the function achieve adequate power for the many planets at around $T_{eq} \approx 1300$ K, yet avoid exceeding 5% for the hottest planets, which would exceed the bounds of our grid. Such constraints are difficult for the power-law to achieve. Regardless, as a result of its overestimate of high T_{eq} radii, this model had a comparatively disfavorable DIC.

position and inflation power using the GP model. The predictions align well with planets of similar mass and temperature. The shape of $\epsilon(F)$ presented by the GP is corroborated by comparison of the DIC values. Of the parametric models, the Gaussian model is most favored, with a DIC of -1722. The logistic model was next, at -1674, followed by the power-law model at -1641. We interpret this to mean that ϵ decreases towards zero at high fluxes with high statistical significance, in agreement with our conclusions from the GP approach. The DIC of the GP model is -1723, so there is no significant preference between it and the Gaussian model. We present the Gaussian model since it takes a simple analytic form, as a percent of flux and with flux in units of $\text{Gerg s}^{-1} \text{ cm}^{-2}$:

$$\epsilon = (2.35^{+1.3}_{-.25}) \text{Exp} \left[-\frac{(\log(F) - (.13^{+.063}_{-.061}))^2}{2 (.37^{+.035}_{-.060})^2} \right] \quad (33)$$

To visualize why the Gaussian model is preferred, we compute the posterior predictive radius distributions, and compare them to the radii of our observed planets.

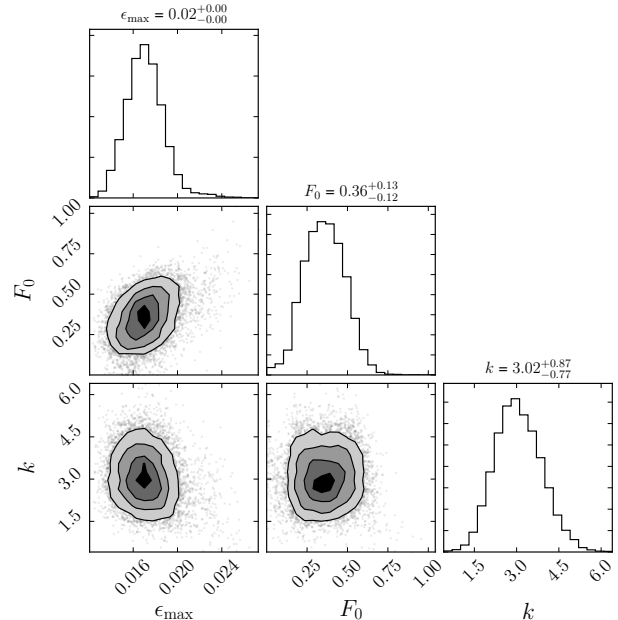


Figure 10. A scatterplot matrix of the logistic function hyperparameter posterior (see eq. 17). Thanks to our prior on k , which demanded the transition be similar to the scale of the data, the resulting posterior is well-behaved and easy to sample from. The model is not bad, but its DIC indicates that it is still inferior to a model which decreases at high equilibrium temperatures.

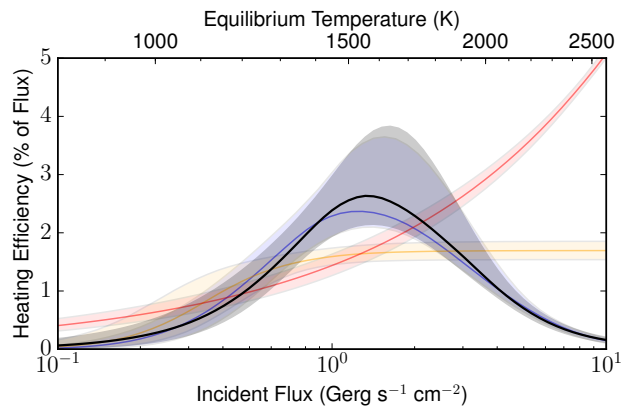


Figure 11. The posteriors of our statistical models of inflation power (as a percent of flux) against incident flux, with 1σ uncertainty bounds. The red line is a power-law model, yellow is logistic, blue is Gaussian, and black is the GP. The Gaussian model is strongly favored over the other parametric models by the DIC model selection criterion, and the GP strongly indicates a negative relationship at high flux. This decrease in inflation efficiency at higher fluxes is important, because it matches predictions from the Ohmic dissipation mechanism of hot Jupiter inflation.

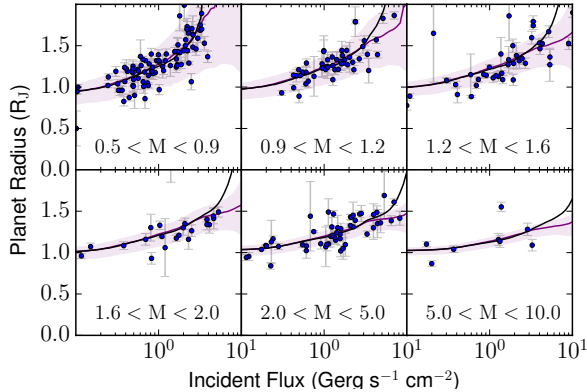


Figure 12. The radii of transiting giant planets against flux, divided into six mass bins. The blue line and region are the GP predicted radius and 1σ uncertainty bounds. The black line is the prediction for the next best model, the logistic function. The latter makes similar predictions but over-predicts radii of high flux planets, so the DIC favors the GP model by a statistically significant margin. This is more obvious looking directly at the residuals, which are shown in Fig. 13.

Figure 12 compares these predictions for the favored GP model and the next-best logistic model to the observed radii as a function of incident flux, divided into six mass bins. The models only diverge at high fluxes, about $2 \text{ Gerg s}^{-1} \text{ cm}^{-2}$. Beyond this, the logistic model systematically overestimates the radii, and the GP does not. To make this clear, Figure 13 shows the residual to the expected radius (the radius anomaly) for high fluxes under a no inflation model, the logistic model, and the Gaussian model. Here, the increasing bias of the logistic model for the 30 planets at such high fluxes is apparent. Even a flat ϵ at high flux predicts overly large planets, hence our conclusion that $\epsilon(F)$ must decline.

For our model of thermal tides (Arras & Socrates 2009), we examined the scaling relations for thermal tides from Socrates (2013), and found this potential power source to much too strongly increase with flux to reproduce the observed radii. The variance also appears overly high; for example, the scaling relations force ϵ to vary by more than an order of magnitude just in planets with fluxes between 0.8 and $1.2 \text{ Gerg s}^{-1} \text{ cm}^{-2}$. As a result, we encountered considerable difficulty getting the model (see section 4.1) to fit. We were only able to fit a model by imposing the regularizing constraint that ϵ for any individual planet cannot exceed 4.5%, a level far above what is otherwise needed to explain the observed radii. Under this requirement, we measure $\log_{10}(\epsilon_0) = -1.61 \pm .064$, Figure 14 shows the the inferred heating efficiencies for the sample planets as a function of flux. The MCMC was able to fit the bulk

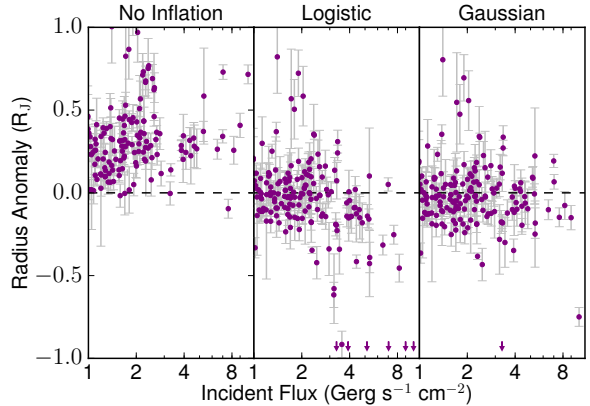


Figure 13. The difference between observed and predicted radius plotted against incident flux assuming typical composition planets under the cool giant model (no inflationary effect), the logistic model, and the Gaussian model (see Fig. 11). Arrows show the handful of planets where the model exceeded the observed radius by more than $1 R_J$, which typically occurs only for very hot, very low mass planets whose radii are extremely sensitive to bulk metallicity. Heavy-element abundance variations Thorngren et al. (2016) are sufficient to explain the scatter (see Fig. 12). Error-bars depict observational error only. The plot illustrates why our statistical tests prefer the Gaussian model over the logistic model: the logistic model consistently overestimates the radii of planets at high fluxes, while the Gaussian model does not.

of the data by placing them in the .5 – 3% range, but the scaling is far too extreme. In explaining the bulk of the planets, a huge 45% (122/281) of the data exceeded the upper bound. Without the constraint, very few of the planets actually end up inflated; the range of coefficients to ϵ_0 given by the scaling relation from Socrates (2013) is simply too large. As such, we conclude that the dominant source of inflation power in the observed population does not follow the thermal tides scaling relation.

6. DISCUSSION

The Gaussian shape is significant because it exclusively matches predictions of hot Jupiter inflation from the Ohmic dissipation mechanism. Under this model, magnetic interactions transfer energy from the atmosphere of a planet into its interior (Batygin & Stevenson 2010). The effect is initially increasing with greater atmospheric temperatures and therefore ionization, but at very high temperatures the magnetic drag on atmospheric winds (Perna et al. 2010) inhibit the process (Menou 2012; Batygin et al. 2011). Batygin et al. (2011) predicts a scaling with equilibrium temperature as $\epsilon \propto (1500\text{K}/T_{\text{eq}})^4$. Menou also derives scaling laws for this effect, estimating the peak ϵ to occur at 1600 K, depending on the planetary magnetic field strength

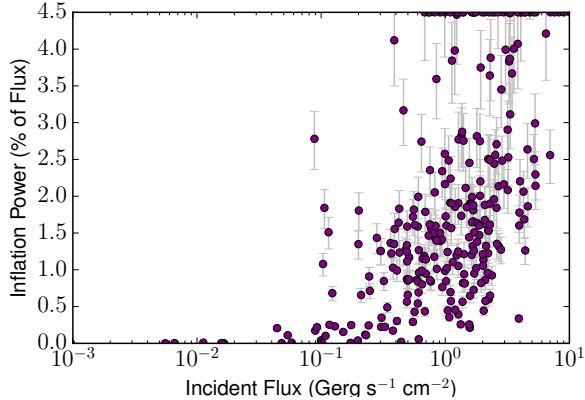


Figure 14. The posterior heating efficiencies for our sample planets as a function of flux, using the thermal tides scaling relationship from [Socrates \(2013\)](#) but leaving a constant scaling factor as a fit parameter. The match with observations was poor, as it forces ϵ to vary by orders of magnitude in ways not apparent in the planet radii. The DIC was -1642, the worst of the models we have tried, though this was likely affected by our constraint that $\epsilon < 4.5\%$. A large fraction of the data (44% or 122/281) exceeded this upper bound and was clipped down to 4.5%.

([Menou 2012](#)). [Ginzburg & Sari \(2016\)](#) supports this conclusion, estimating a peak ϵ to occur at 1500 K, with power-law tails on either side. Figure 11 shows that the posteriors of our favored models match these predictions well. If Ohmic dissipation is responsible for our observation, then our measured $\epsilon(F)$ is presumably the average over various planetary magnetic field strengths.

A noteworthy difficulty with identifying our results with the Ohmic dissipation model is the depth at which the anomalous heat is deposited. Our model assumes that anomalous heating is efficiently conducted into the interior adiabat. Ohmic heating, however, is generally believed to be deposited at pressures low enough that only a portion of the deposited energy is inducted into the adiabat and a delayed cooling effect is produced ([Spiegel & Burrows 2013](#); [Wu & Lithwick 2013](#); [Komacek & Youdin 2017](#)). As well as differing from our modeling assumptions, this appears inconsistent with the results of [Hartman et al. \(2016\)](#), who observe re-inflation of giants as their parent stars age and brighten over their main-sequence lifetime. This effect would be prohibitively slow in the shallow deposition case ([Ginzburg & Sari 2016](#)). Thus if Ohmic heating is to explain our results, it must either violate these predictions or be modified by an additional effect which ushers the heat further into the planet. The advection effects proposed by [Tremblin et al. \(2017\)](#) show that such effects are plausible and that there is still a great deal left to understand about atmospheric flows in hot Jupiters.

As the results of [Tremblin et al. \(2017\)](#) stand, our observations do not seem to support them as the sole cause of inflation. They predict observable inflation occurring well below the observed $0.2 \text{ Gerg s}^{-1} \text{ cm}^{-2}$ threshold, and do not appear to support a decrease in efficiency at high flux. However, our results might align better if temperature-dependent wind speeds are considered within their model, which could slow flows both at especially low and high T_{eq} .

Other candidate inflation models do not match our results very well. Tidal heating may introduce non-negligible energy into planet interiors, but cannot fully explain the anomalous radii ([Miller et al. 2009](#); [Leconte et al. 2010](#)), and would not reproduce our relationship with flux. The thermal tides mechanism ([Socrates 2013](#)) appears to predict more variation in ϵ than can plausibly exist (see Fig. 14). Delayed cooling models propose that no anomalous heating occurs and that radii anomalies instead result from phenomena which prevent the escape of formation energy, such as enhanced atmospheric opacities ([Burrows et al. 2007](#)) or inefficient heat transport in the interior ([Chabrier & Baraffe 2007](#)). This energy would otherwise rapidly radiate away. The issue with these proposals is that they do not inherently depend on flux and cannot explain the results of [Hartman et al. \(2016\)](#).

The situation for Saturn-mass planets (those excluded from our model) remains puzzling. As described in Section 2, these exhibit a different relationship with flux than Jupiter mass planets (Fig. 2) and have been found less frequently in high flux orbits than their higher-mass analogs (Fig. 3). Inefficiency in the heating mechanism, perhaps by lower magnetic field strengths, could explain the former observation, but not the latter. Furthermore, [Pu & Valencia \(2017\)](#) recently showed that Ohmic dissipation should occur in Neptunes, so we can reasonably expect that it would work on Saturns as well. Some observational biases are doubtless present, but would likely not produce the effects seen. Thus it seems possible that mass loss is occurring. However, the exact mechanism would be unclear; for example, neither XUV driven mass-loss ([Yelle 2004](#); [Lopez et al. 2012](#)) nor boil-off ([Owen & Wu 2016](#)) appear to significantly affect planets in this mass range. As such, the cause of these observations is an open question.

There is still much work to be done in understanding hot Jupiter radius inflation. A promising avenue are the case of “reinflated” hot Jupiters, which are planets whose radii may be increasing over time as their stars evolve off the main sequence and brighten ([Lopez & Fortney 2016](#)). [Grunblatt et al. \(2017\)](#) have conducted promising observations of two potentially re-

inflated planets around sub-giant stars. Our posterior radius predictions are closer to their observations under the re-inflated case, but more planets will be needed to establish strong statistical significance. Comparing the main-sequence reinflation results of [Hartman et al. \(2016\)](#) with structure models could reveal the timescale of re-inflation, which is closely related to the depth of energy deposition ([Komacek & Youdin 2017](#); [Ginzburg & Sari 2016](#)). If re-inflation does indeed occur, delayed cooling models are ruled out. Follow-up work of [Tremblin et al. \(2017\)](#) to determine how their results would be affected by temperature-dependant wind speeds would also be helpful. Finally, further magnetohydrodynamic

simulations are needed to properly understand heat flow in the outer layers of these planets. Our results add to this picture by providing strong evidence of a heating efficiency drop at high temperatures and thereby pointing us towards the Ohmic dissipation model; they also suggest that 3-D atmosphere models need to take magnetic fields into account.

The authors thank Eric Lopez, Vivien Parmentier, Thad Komacek, and Ruth Murray-Clay for helpful discussions. Funding for this work was provided by NASA XRP grant NNX16AB49G.

REFERENCES

- Akeson, R. L., Chen, X., Ciardi, D., et al. 2013, *PASP*, 125, 989
- Arras, P., & Socrates, A. 2009, ArXiv e-prints, arXiv:0901.0735
- Baraffe, I., Selsis, F., Chabrier, G., et al. 2004, *A&A*, 419, L13
- Batygin, K., & Stevenson, D. J. 2010, *ApJL*, 714, L238
- Batygin, K., Stevenson, D. J., & Bodenheimer, P. H. 2011, *ApJ*, 738, 1
- Burrows, A., Hubeny, I., Budaj, J., & Hubbard, W. B. 2007, *ApJ*, 661, 502
- Chabrier, G., & Baraffe, I. 2007, *ApJL*, 661, L81
- Charbonneau, D., Brown, T. M., Latham, D. W., & Mayor, M. 2000, *ApJL*, 529, L45
- Demory, B.-O., & Seager, S. 2011, *ApJS*, 197, 12
- Foreman-Mackey, D. 2016, *The Journal of Open Source Software*, 24, doi:10.21105/joss.00024
- Fortney, J. J., Marley, M. S., & Barnes, J. W. 2007, *ApJ*, 659, 1661
- Gelman, A., Hwang, J., & Vehtari, A. 2014, *Statistics and Computing*, 24, 997
- Ginzburg, S., & Sari, R. 2016, *ApJ*, 819, 116
- Grunblatt, S. K., Huber, D., Gaidos, E., et al. 2017, ArXiv e-prints, arXiv:1706.05865
- Guillot, T., & Showman, A. P. 2002, *A&A*, 385, 156
- Hartman, J. D., Bakos, G. Á., Bhatti, W., et al. 2016, *AJ*, 152, 182
- Hastings, W. K. 1970, *Biometrika*, 57, 97
- Henry, G. W., Marcy, G. W., Butler, R. P., & Vogt, S. S. 2000, *ApJL*, 529, L41
- Hubbard, W. B., Hattori, M. F., Burrows, A., Hubeny, I., & Sudarsky, D. 2007, *Icarus*, 187, 358
- Kass, R. E., & Raftery, A. E. 1995, *Journal of the American Statistical Association*, 90, 773
- Komacek, T. D., & Youdin, A. N. 2017, ArXiv e-prints, arXiv:1706.07605
- Laughlin, G., Crismani, M., & Adams, F. C. 2011, *ApJL*, 729, L7
- Leconte, J., Chabrier, G., Baraffe, I., & Levrard, B. 2010, *A&A*, 516, A64
- Lopez, E. D., & Fortney, J. J. 2016, *ApJ*, 818, 4
- Lopez, E. D., Fortney, J. J., & Miller, N. 2012, *ApJ*, 761, 59
- Menou, K. 2012, *ApJ*, 745, 138
- Miller, N., & Fortney, J. J. 2011, *ApJL*, 736, L29
- Miller, N., Fortney, J. J., & Jackson, B. 2009, *ApJ*, 702, 1413
- Owen, J. E., & Wu, Y. 2016, *ApJ*, 817, 107
- Perna, R., Menou, K., & Rauscher, E. 2010, *ApJ*, 719, 1421
- Pu, B., & Valencia, D. 2017, *ApJ*, 846, 47
- Saumon, D., Chabrier, G., & van Horn, H. M. 1995, *ApJS*, 99, 713
- Schneider, J., Dedieu, C., Le Sidaner, P., Savalle, R., & Zolotukhin, I. 2011, *A&A*, 532, A79
- Silverman, B. W. 1986, *Density estimation for statistics and data analysis*
- Socrates, A. 2013, ArXiv e-prints, arXiv:1304.4121
- Spiegel, D. S., & Burrows, A. 2013, *The Astrophysical Journal*, 772, 76
- Spiegelhalter, D. J., Best, N. G., Carlin, B. P., & Van Der Linde, A. 2002, *Journal of the Royal Statistical Society: Series B (Statistical Methodology)*, 64, 583
- Thompson, S. L. 1990, ANEOS—Analytic Equations of State for Shock Physics Codes, Sandia Natl. Lab. Doc. SAND89-2951
- Thorngren, D. P., Fortney, J. J., Murray-Clay, R. A., & Lopez, E. D. 2016, *ApJ*, 831, 64
- Tremblin, P., Chabrier, G., Mayne, N. J., et al. 2017, *ApJ*, 841, 30

Van Der Walt, S., Colbert, S. C., & Varoquaux, G. 2011,

ArXiv e-prints, arXiv:1102.1523

Weiss, L. M., Marcy, G. W., Rowe, J. F., et al. 2013, ApJ,
768, 14

Wu, Y., & Lithwick, Y. 2013, The Astrophysical Journal,
763, 13

Yelle, R. V. 2004, Icarus, 170, 167